Supplementary Information

Contents

Supplementary methods

Computational model

The computational model used is based on the model previously published by Farhadifar et al. 2007 and previously used by us in Mao et al. 2011. The model was extended in several ways for the purposes of this paper.

Energy of the system

Firstly, we simplified the underlying equation for the energy of the system, dropping the perimeter contractility terms. Such that the expression for the energy became:

$$E(R_i) = \sum_i \frac{1}{2}\left(A_\propto - A_\propto^{(0)}\right) + \Lambda \sum_{<i,j>} \left(1 + \varphi_{ij}^{Dachs}\right) l_{ij}$$

(for detailed explanations about this equation and the parameters used please refer to our previous paper, Mao et al. 2011). The line tension parameter was reparametrised using the same benchmarks we used previously (see Mao 2011), we obtained and used Λ= 0.26.

Global vs local friction

Secondly, in order to distinguish between global frictional forces and forces due to the local viscosity of the acto-mysosin cortex, at each step of the simulation, the set of equations corresponding to the presence of these two frictional components was solved:

$$\overrightarrow{F_i} = f_{global}\vec{v}_i + f_{local}\vec{v}_{i,local}$$

Where $\overrightarrow{F_i}$ is the force acting on vertex *i*, f_{global} is the global friction due to the presence of the ECM and viscous medium and f_{local} is the local friction due to the viscosity of the acto-myosin cortex. $\vec{v}_{i,local}$ is the local velocity of vertex *i*, defined as

$$\vec{v}_{i,local} = \vec{v}_i \ - \langle \vec{v}_k \rangle_{neighbours}.$$

As previously the program was written in C++ and in order to render the computational problem tractable the equations were written as a sparse matrix problem and solved at each step using the optimized sparse matrix operation library from Intel (MKL libraries, Intel's optimized implementation of the sparse matrix PARDISO solvers).

The local viscosity term was parametrised using experimental laser ablation data. Whereas the short-term behavior of the recoil data relates to the tension in the system, the long term behavior of the recoil data relates to the viscosity of the medium as experienced by the vertices. Assuming elastic behavior with friction from the environment yields an exponential relationship for the long term behavior of the form, $f(t) = A(1 - e^{-\frac{k}{\mu}t})$, where *k* is the spring constant of the actomyosin cortex and μ the friction exerted by the medium on the motion of the vertex. Fitting such a curve to the experimental data we were able to extract a unique value for the ratio $\frac{k}{\mu}$. Reproducing laser ablations *in silico* we were then able to reproduce recoil curves corresponding to the experimental laser ablation data. We fitted the data to obtain the corresponding $\frac{k}{\mu}$ ratios. Varying the value f_{local} of the local friction in the model, we were thus able to obtain a value for the local friction in the model, $f_{local} = 33$ a.u., which reproduces the experimental laser ablation long term behavior. The global friction was generally assumed to be negligible and was, for most scenarios, kept at values which did not have any influence on the final results (<1 a.u.).

Parameters for the different scenarios

Dachs was present in all scenarios. We generally used the value φ_{max}^{Dachs} = 0.153 as parametrised in our previous paper Mao et al 2011.

Local friction was generally set to 33 a.u. whereas the global friction was set to 1% of the local friction, i.e. 0.33 a.u..

Cells divided along their long axis.

Line tension term was Λ= 0.26.

Uniform proliferation scenario
As above.

Constriction belt scenario

The vertices of the cells on the outer periphery were assigned a much higher global friction coefficient of 200 a.u.. The local friction algorithm was very unstable in this setup and was not used.

High friction scenario
The global friction was set to 1000 a.u.. The global friction completely overruled the local friction, so we did not use the local friction algorithm in this setup.

Differential proliferation scenarios
Cell division were driven using a duration for the G1/S phase varying as a function of the relative distance to the center, *r* :

$$\Delta t_{Go}(r) = A\left(1 + e^{-k(RW-r)}\right)$$

with parameters *A*=4 , *k*=5 , *RW*=0.3.

Figures S6 D and E present the effective proliferation rates calculated using clonal lineage following the method used in the *in vivo* experiments.

For the gentle proliferation differential presented in Figures 7E,F we used *k*=3.

For the *in vivo* differential proliferation profile (Figs 7I-M) we used φ_{max}^{Dachs} = 0.3 and a linear proliferation profile designed to mimic the experimental values (Fig 7A-D):

$$\Delta t_{Go}(r) = A - (A - B)r$$

With:

A = 3.5	and	*B* = 2	for 18 hours, followed by
A = 3	and	*B* = 2	for 18 hours, followed by
A = 1.8	and	*B* = 1.8	for 12 hours, followed by
A = 1.2	and	*B* = 1.2	for 24 hours.

Image analysis: Automated Image Segmentation Method

Drosophila wing discs are labelled with E-cadherin::GFP. Image stacks were acquired on a Leica SP5 Confocal Laser Scanning microscope with Z intervals of 0.5 (fixed samples), or a Perkin Elmer Spinning Disc Microscope (live imaging).

Image stacks of the Drosophila wing disc (Fig. S7A) represented a dome shaped surface consisting of two cellular layers within the image volume: a dense mesh corresponding to the wing disc proper cells of interest and a less dense mesh corresponding to the peripodial cells. The aim of the image processing method was to separate these two layers and to determine and analyse the morphometric characteristics of the apical region of the wing disk epithelial cells.

The image processing was performed in several steps. Firstly, the wing disc epithelial mesh was extracted from the image volume in the form of a 2D projection by fitting a continuous surface (using Matlab method Gridfit 2005) through the parts of the image with the strongest intensity, corresponding to the apex of the wing disk epithelium. Although the surface obtained generally coincided to the wing disc proper, in many instances membrane junctions belonging to the peripodial cells would be picked up by the surface fitting. It was possible to reduce this problem by increasing the stiffness of the fitted surface, which would then follow the denser disc epithelium mesh and thus ignore the peripodial cells. This was especially a problem with younger discs where the two layer have not yet fully differentiated, in this case we manually adjusted the surface so as to acquire the correct cell layer. The pixel intensities along the fitted surface formed the projection on which the subsequent image segmentation was performed. Fig. S7B depicts an example of a projection image.

The resulting projection images were first de-noised using a simple Gaussian smoothing operation. The image segmentation was then performed by growing cellular regions from individual seed points. In a first step, seed points were automatically identified as small, homogeneous regions within the projection image. Fig. S7C shows the projection image with overlaid seed points. These seed points were then grown concurrently using a newly written hill climbing technique to form regions. However, large cells could express more than one seed point, which would lead to an incorrect segmentation. Therefore, in a next step, seeds with weak boundaries between them were merged. Fig. S7D depicts the projection image with overlaid seeds after the merging procedure. In a final step, the remaining seeds were grown concurrently on the original projection image using the same hill climbing technique to result in regions corresponding to individual disc proper cells. Fig. S7E shows the resultant cellular regions with seeds and boundaries overlaid after the final growing procedure. The boundaries of these cellular regions were then extracted for the analysis of cell area, orientation, shape and position. The curvature of the projection surface was taken into account for these measurements. Visual inspection and manual correction of the seeding was performed on the individual discs prior to analysis.

T1 transitions analysis

The T1 transitions were analysed in the following way. Microscopy image stacks of individual live *ex vivo* cultured imaginal discs (staged 100 hours after egg laying) were collected every 5 minutes over a 5 hour period. The individual z-stacks were projected and segmented in the way presented above. This segmentation was then used to track cells over the 5 hour period (each movie required ~1 hour manual correction). The segmentation was then further used to determine the position of vertices defined as the points where 3 or 4 cells meet. This then enabled each time-frame to be described as a collection of cells, each defined as a set of vertices (vertex representation). T1 transition event were then detected by looking for changes in the neighbours of each cells. Any set of 4 cells thus detected has having potentially undergone a T1 transition was then tracked through time. Such T1 tracks can be seen in Fig S8A-C, where the distance of the junction is tracked over time (a negative distance indicates that the T1 transition has taken place and the distance of the new junction is being tracked). As can be seen in Fig S8A-C the transitions were inherently noisy, this could be due to stochastic fluctuations in the recorded microscopy intensities leading to small variations in the segmentation from one frame to the next or might be more biologically relevant fluctuations such as those seen in dorsal closure. From Fig S8A-C it is quite apparent that overall trends appear, which are themselves representative of the true movement of the tissue, whereas the small fluctuations are not. For this reason we fitted straight lines through the data, the slope of which gives us a true indication of the speed at which the tissue is remodelling itself through T1 transitions. Finally, T1 transitions were defined as those time-tracks where the fitted line intersected the x-axis over the 5 hours of the movie (such as Fig S8A-B).

Fig S8D-F presents similar tracks obtained from simulations corresponding to the movies obtained *in-vivo*. Here, we can see that the picture emerging from the *in-silico* modelling is qualitatively different: fluctuations are present but are small compared with the clear and fast T1 transition processes. We therefore decided to use the much steeper slope of the actual transition for the *in-silico* T1 movies.

All image processing and analysis techniques were implemented in Matlab (Mathworks Inc.). The region growing technique was implemented as C extensions for Matlab to reduce processing time. A graphical user interface was developed to manually correct seed positions if necessary. The microscopy data and processed images were stored in an

OMERO database (openmicroscopy.org) accessed through Matlab. These tools are available upon request.

Supplementary References

Gridfit: John D'Errico, Mathworks central, 2005
http://www.mathworks.co.uk/matlabcentral/fileexchange/8998-surface-fitting-using-gridfit

Mao_Figure S1

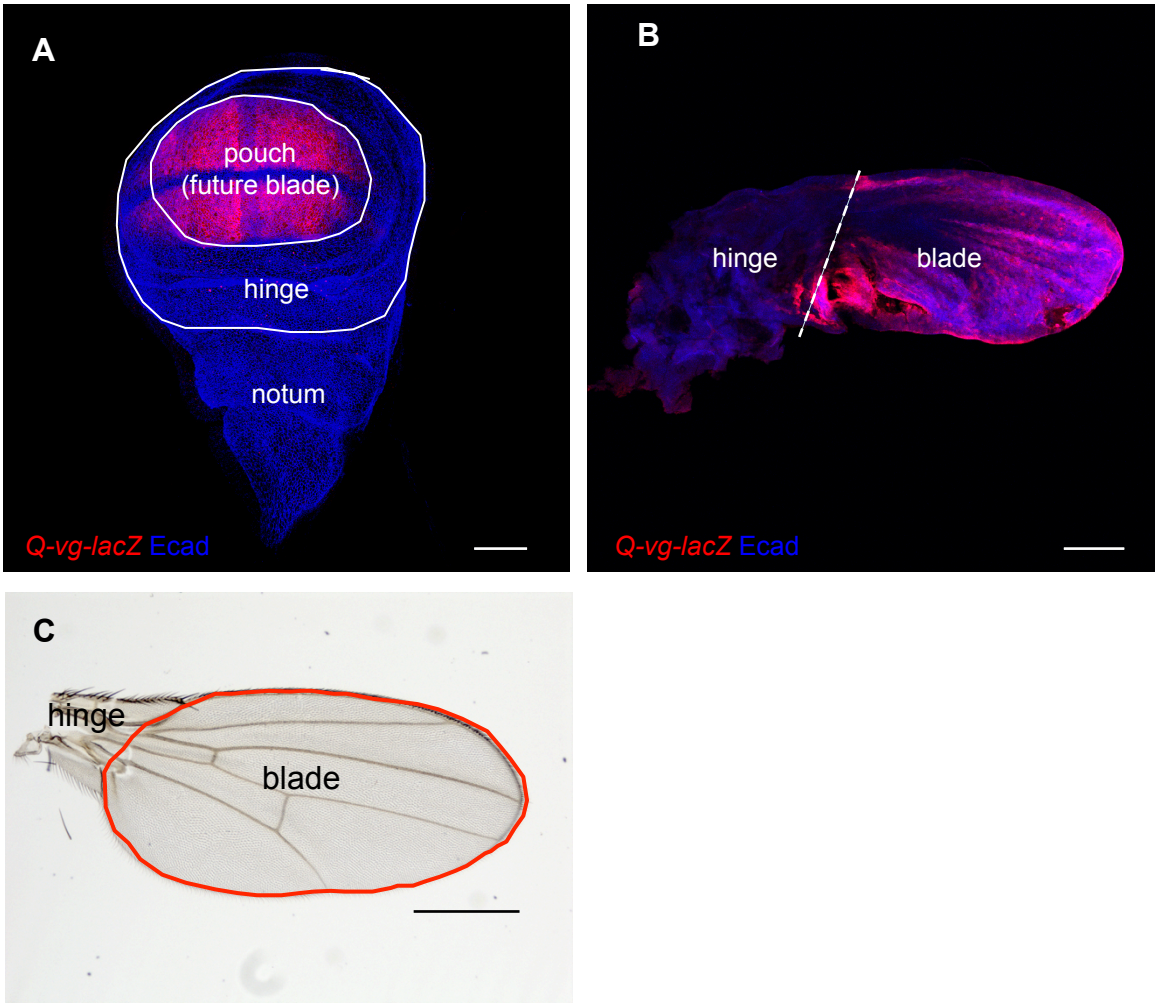

Figure S1. The region of the wing pouch analysed throughout the paper corresponds to the future adult wing blade. **(A)** *Q-vg-lacZ* wing disc (stained with anti-βgal and anti-Ecadherin). The *Q-vg-lacZ* domain marks in late 3rd instar wing discs the exact region of the pouch, up to the first fold, used in the analysis. Scale = 50μm **(B)** The *Q-vg-lacZ* expression pattern can be seen in pupal wings (20h after pupariation) in just the wing blade region, and not the hinge region. Note the notum region, which forms the back of the adult fly, can no longer be seen at this stage in these preparations. Scale = 150μm **(C)** Adult wing blade highlighted in red, scale = 400μm. The *Q-vg-lacZ* flies were a kind gift from Pradip Sinha.

Mao_Figure S2

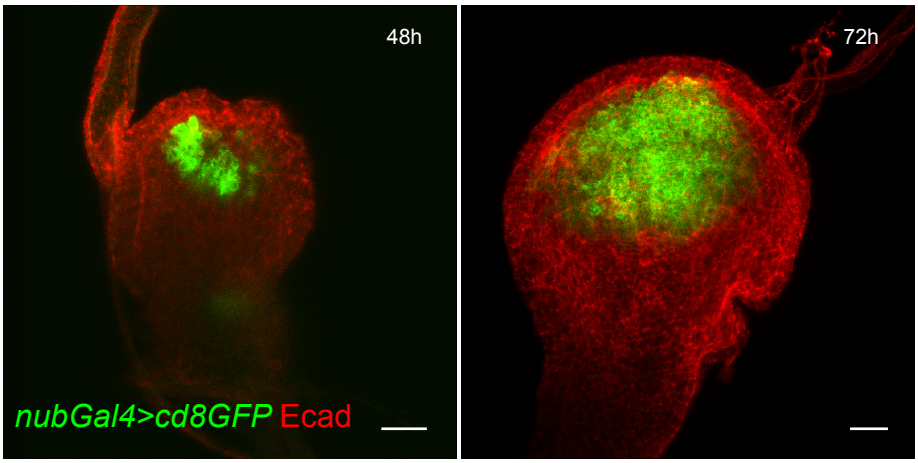

FigureS2. The Nubbin expression domain (*nubbin-Gal4* > *UAScd8GFP*) was used to define the areas of the wing pouch used for the analyses of cell shapes for the 48h and 72h wing discs, before the folds develop. Scale = 15µm. The *nubbin-Gal4* line is available from Bloomington.

Mao_Figure S3

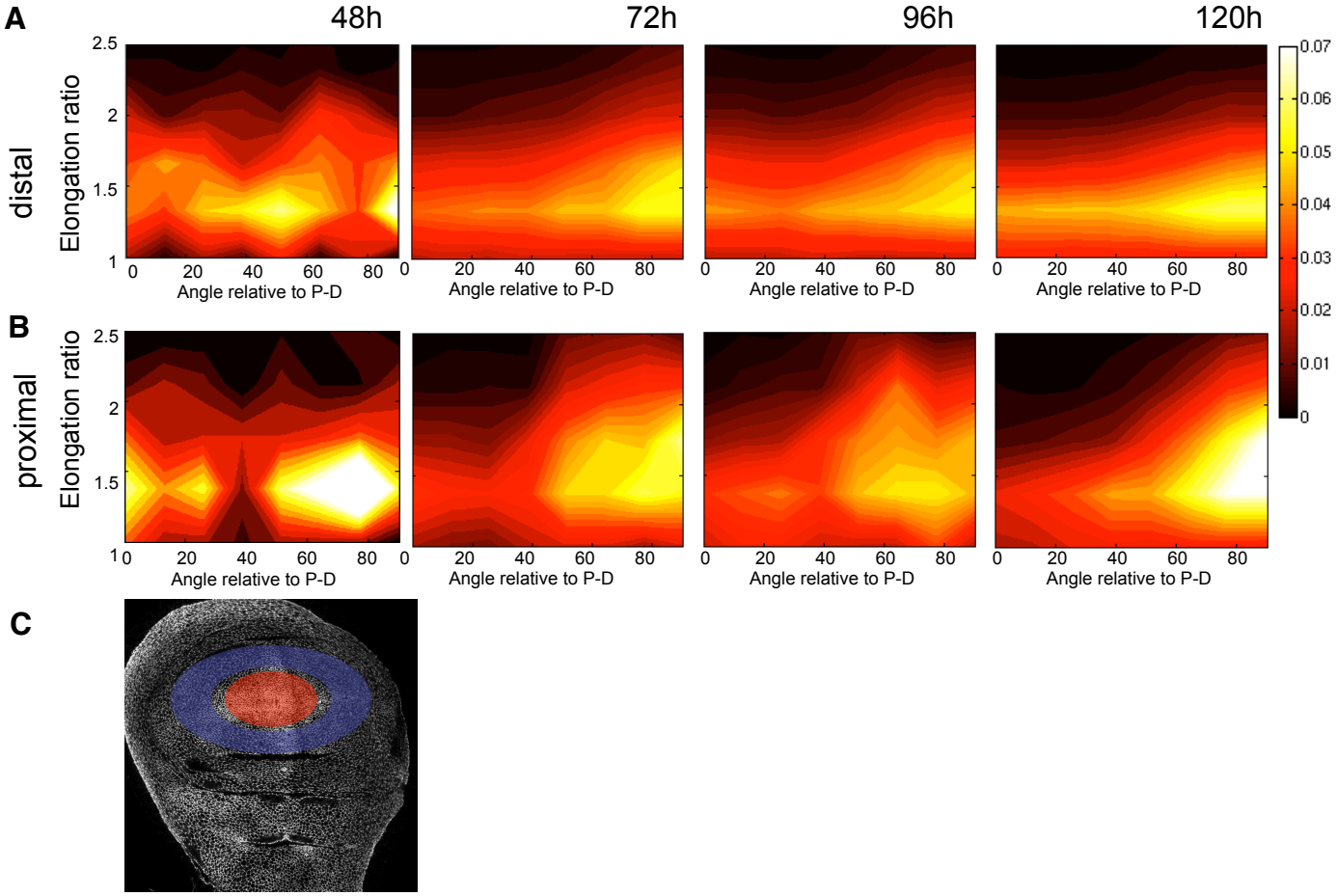

Figure S3. Analysis of cell elongation orientation at different ages in wing discs. In all graphs, Y-axis is the elongation ratio, and X-axis is the orientation of the long axis, relative to the P-D axis. The heat map represents percentage of cells. **(A)** Analysis of cells in the distal (centre) portion of the wing disc, red region in **C**. At steady state, the bias of cell orientations along the P-D axis is not visible, as this is only apparent in cells just prior to mitosis (Fig. 1F). **(B)** In the proximal (edge) portion of the wing disc (blue region in **C**), more cells show further elongation and their orientation is strongly biased perpendicular to the P-D axis. **(C)** The same figure as in Fig. 4C to highlight the distal and proximal zones: distal (red), proximal (blue).

Mao_Figure S4

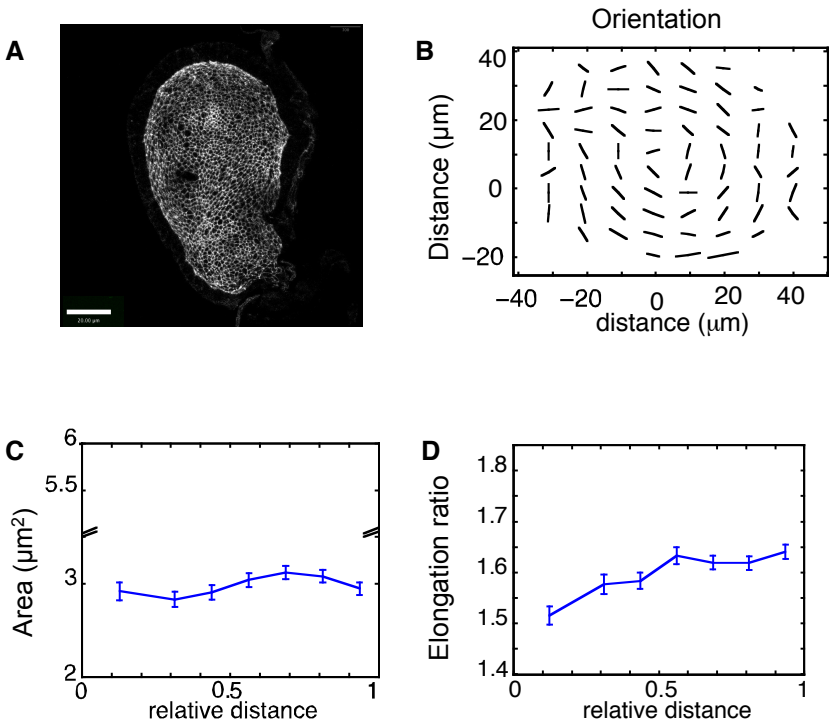

Figure S4. Quantification of wing disc cell topology at 60h after egg laying. **(A)** A single E-cadherin::GFP expressing wing disc to mark apical cell profile. Scale bar = 20μm. **(B-D)** Averaged data from 8 wing discs. (**B)** Cell elongation orientation. Length of bar is proportional to elongation ratio. **(C)** Apical cell area plotted against its relative distance from the centre to the edge of the pouch. **(D)** Elongation ratios of cells plotted against its relative distance from the centre to the edge of the pouch. Error bars indicate s.e.m.

Mao_Figure S5

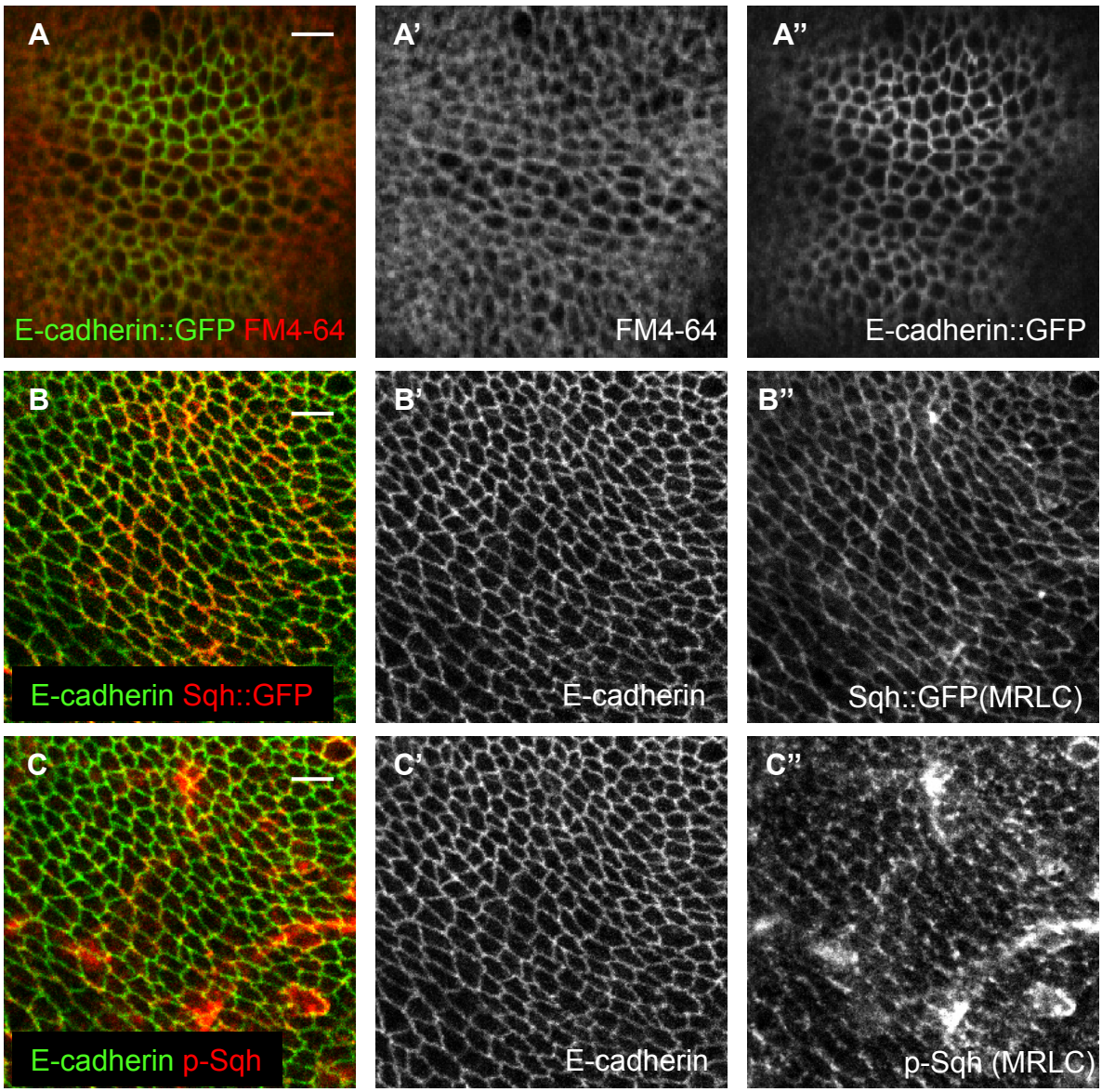

Figure S5. (A) E-cadherin::GFP expressing wing disc stained with FM4-64 dye to label the uniform cell membranes. No clear anisotropy in E-cadherin expression patterns are visible when compared to the FM4-64 pattern. Wing discs were cultured with the FM4-64 dye (Invitrogen) at 10µg/ml for 10 minutes before washing with PBS and imaging live in culture media immediately to preserve the cell shape and stain quality. **(B)** Wing disc expressing Sqh::GFP at endogenous levels showing myosin-II regulatory light chain (MRLC) expression pattern, and stained with anti-E-cadherin. No clear anisotropy in expression levels can be detected in either of the patterns. **(C)** A wing disc stained for phospho-Sqh (p-MRLC, Cell Signalling) to show myosin-II activity and anti-E-cadherin. The proximal/distal edges appear to have higher myosin-II activity. For definition of P/D edges see Fig. 4. Scale = 5µm

Mao_Figure S6

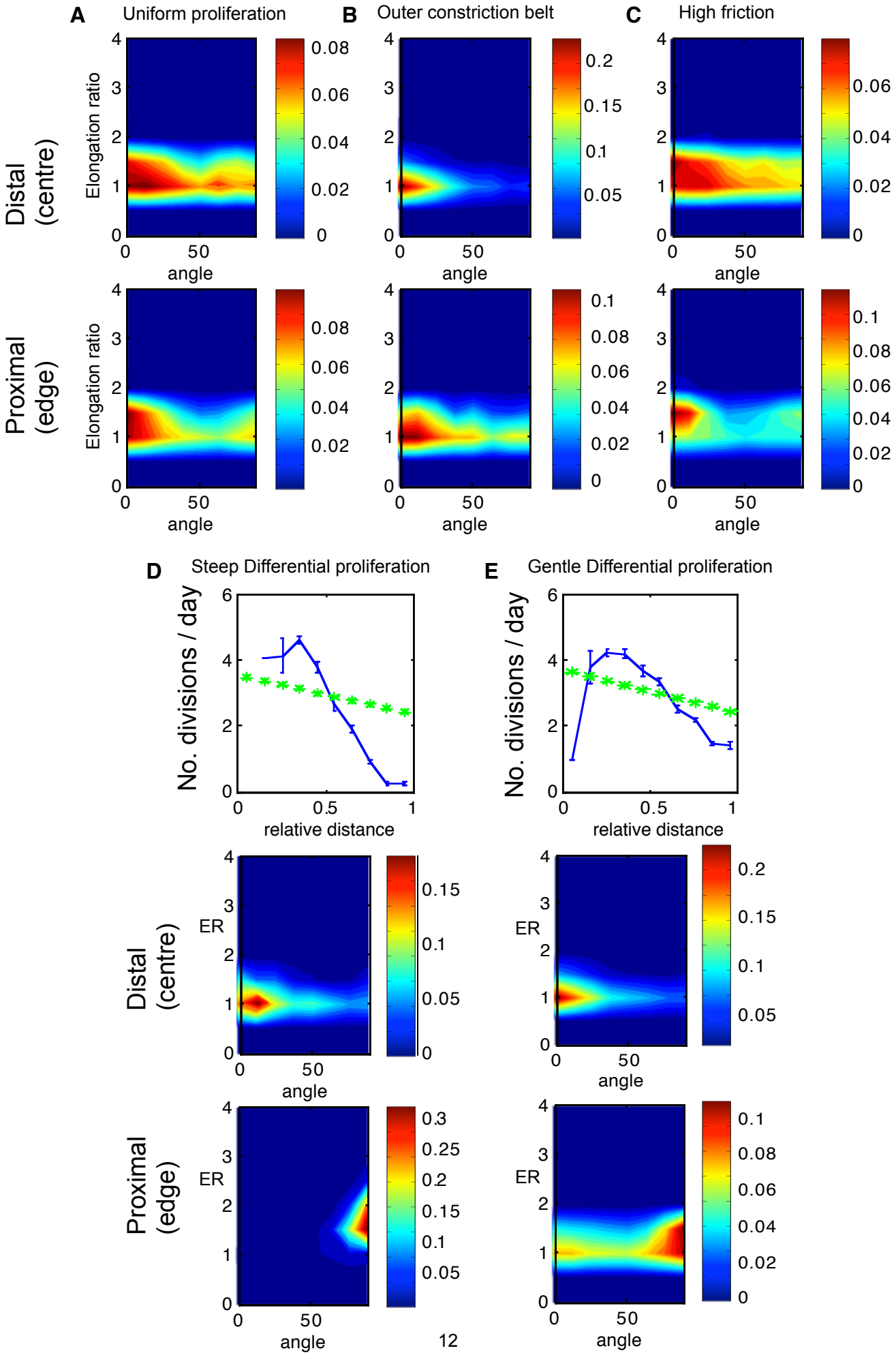

Figure S6. Analysis of cell elongation and orientation for different simulation scenarios. The same analysis as in Fig. S3 is performed. (**A-C**) Although these simulations give slightly elongated cells, their orientations in both the distal and proximal regions are along the P-D axis, and does not match that of *in vivo* wing discs (especially in the proximal region, see Fig. S3B). Y-axis: elongation ratio. X-axis: orientation relative to P-D axis (0^o parallel to P-D, 90^0 is perpendicular to P-D). Heat map represents percentage of cells. **(D-E)** Differential proliferation produces elongated cells in the proximal (edge) region that are also oriented perpendicular to the P-D axis, as *in vivo*. Top panels show the exact proliferation rates used in the simulation (blue line). Green stars show *in vivo* measured proliferation rates for comparison. The steeper the proliferation rate differential, the more elongated the cells become in the proximal edge, but even a shallow differential that closely resembles that of the *in vivo* rate (E) still produces cells that elongate circumferentially at the proximal edge (E bottom panel). Compare with Fig. S3B.

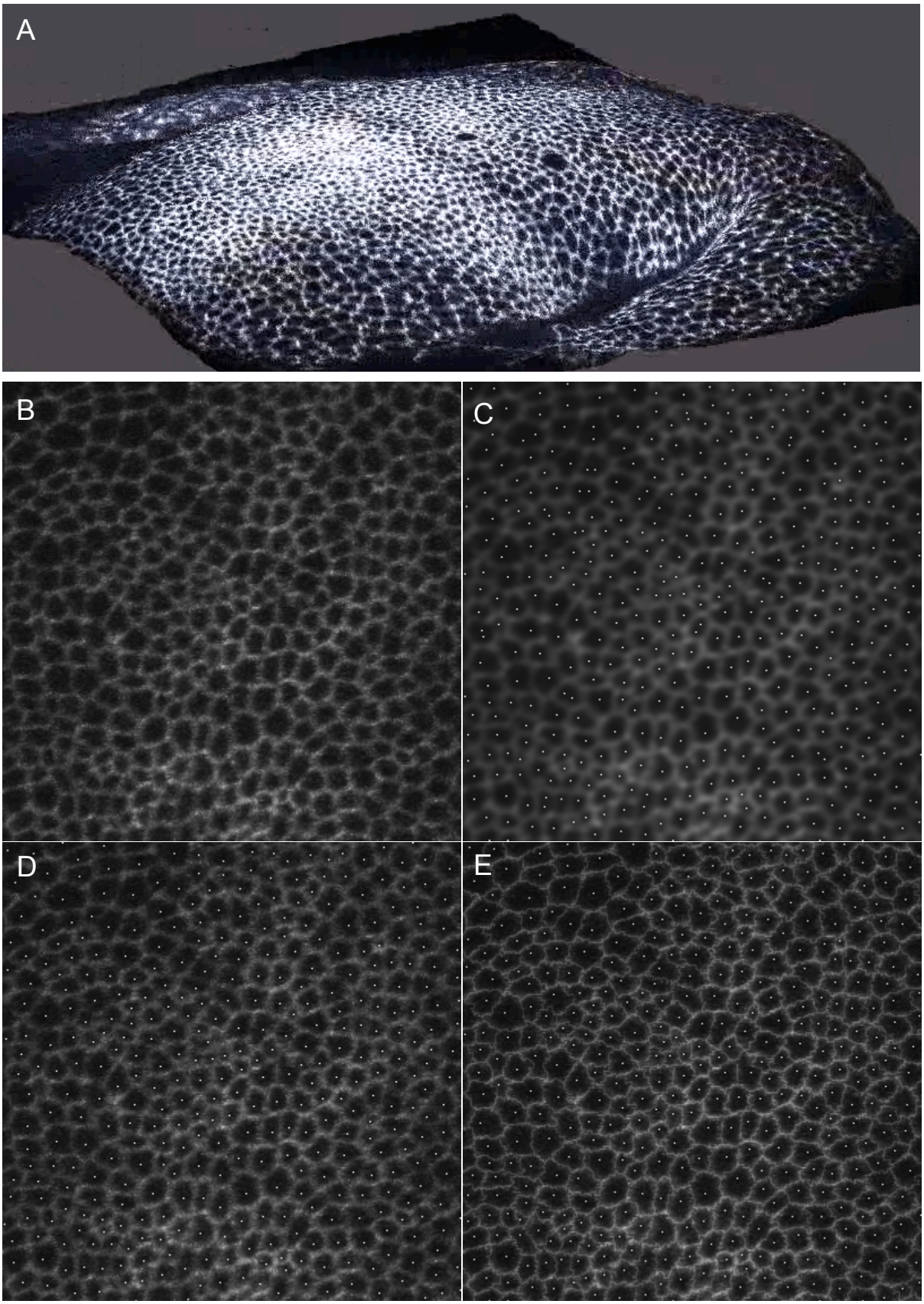

Figure S7. Image segmentation technique. **(A)** A 3-dimensional reconstruction of a *Drosophila* wing disc labelled with E-cadherin::GFP, showing the characteristic dome shape. Projection image **(B)**, overlaid with original seed points after region growing **(C)**, overlaid with seed points after merging **(D)** and the final cell boundary segmentation after region growing **(E)**. See Supplementary Materials and Methods for details of the technique.

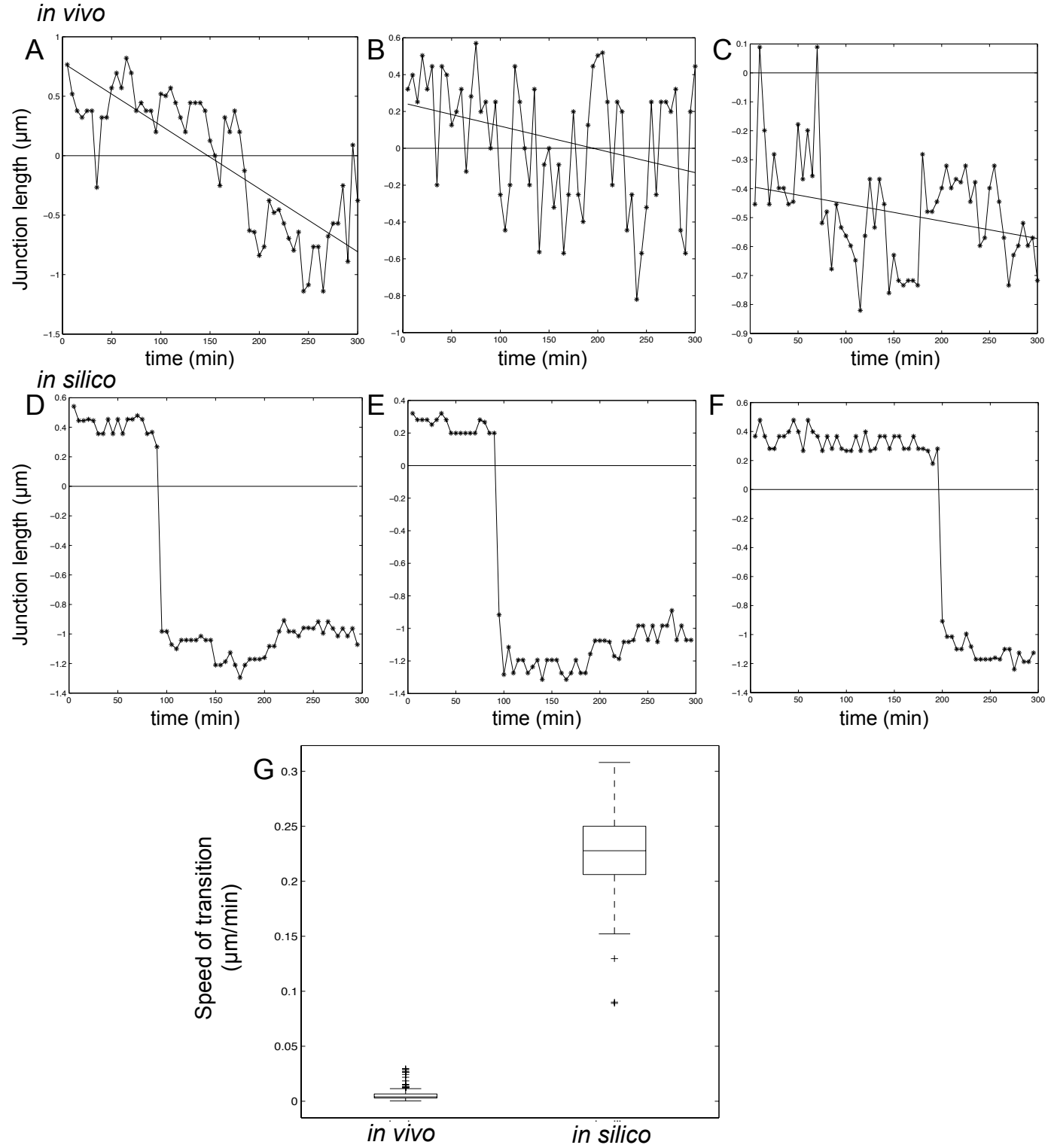

Figure S8. Comparing T1 transitions *in vivo* and *in silico*. **(A-C)** Typical traces of individual cell junction lengths from tracking *in vivo* movies (see Sup. Materials and Methods, Movie S9). Junctions fluctuate in length around 0 (4 cell vertex) and transitions are frequently reversed or unstable. Generally, the T1 transitions *in vivo* occur very slowly, if at all, and appear to be a passive 'indecisive' event as a result of the packing geometry of the tissue. **(D-F)** The *in silico* transitions occur much faster and more decisively and are stably maintained once they do occur, suggesting an active/directed mechanism. **(G)** The 'speed of transitions', n=228 *in silico*, n=300 *in vivo.* Overall this analysis suggests that the *in silico* model is much more plastic in allowing T1 transitions than the *in vivo* tissue, which appears to resists active junctional remodelling.

Mao_MovieS1.
Wing disc expressing Armadillo::GFP staged around 100h AEL.

Mao_MovieS2.
Laser ablation of a P/D junction located in the distal central region of a wing disc around 100h AEL.

Mao_MovieS3.
Simulation of the effect of having uniform proliferation rates.

Mao_MovieS4.
Simulation of the effect of having an outer constriction belt.

Mao_MovieS5.
Simulation of the effect of high uniform friction.

Mao_MovieS6.
Simulation of having a steep differential proliferation gradient, high in the centre, low at the edge.

Mao_MovieS7.
Laser ablation of a junction bordering *wts* mutant clones marked by lack of RFP and also expressing E-Cad::GFP throughout. After the cut, the focus is moved more basally to visualise the nuclear RFP signal.

Mao_MovieS8.
Simulation using *in vivo* measured differential proliferation rates.

Mao_MovieS9.
The final output of the automated image segmentation and cell tracking analysis performed on a wing disc expressing Ecad::GFP around 100h AEL. Individual cells and junctions are identified and accurately tracked over time.